International Journal of
aeroacoustics volume 5 · number 4 · 2006 – pages 311 – 333

Attenuation of slat trailing edge noise using acoustic liners

Zhaokai Ma*, Malcolm G. Smith, Simon K. Richards*** and Xin Zhang*****

**School of Engineering Sciences, University of Southampton, Southampton SO17 1BJ, U.K.*
E-mail:mazhk@soton.ac.uk
***Institute of Sound and Vibration Research, University of Southampton, Southampton SO17 1BJ, U.K.*
E-mail:mgs@isvr.soton.ac.uk
****School of Engineering Sciences, University of Southampton, Southampton SO17 1BJ, U.K.*
E-mail: s.k.richards@soton.ac.uk; xzhang@soton.ac.uk

ABSTRACT

Noise generated by high-lift devices such as the slats on the leading edge of a wing is a major contributor to the overall airframe noise during the landing approach of a commercial aircraft. In this work the concept of attenuating noise sources located at the trailing edge of a slat using absorptive acoustic liners in the slat gap is explored using a time-domain computational aeroacoustic (CAA) scheme. The aim of the computational modelling is to demonstrate the feasibility of controlling slat noise using acoustic liners, and to optimize the design for a future experiment. A model scale three-element high-lift airfoil is modelled; the slat and flap deflection angles are 23 deg and 32 deg respectively and the slat has a blunt trailing edge. The freestream Mach number is 0.2 and the main element angle of attack is 5 deg, corresponding to a typical approach condition. The Reynolds number is 3.6 million, based on the airfoil chord with the high-lift devices retracted.

The computational results are divided into three parts: (1) an unsteady Reynolds-Averaged Navier-Stokes (URANS) simulation using high-order spatial and temporal schemes is conducted for a wing without acoustic liners; the computed flow shows the presence of vortex shedding and acoustic sources behind the slat trailing edge; (2) a calculation of the radiated sound field is made for a range of liner impedance values by solving the linearised Euler equations (LEE) for a modelled acoustic source located at the trailing edge of the slat; (3) URANS computations for the wing with liner treatment are conducted. The results show that acoustic liners on the slat cove and on the main element can provide useful attenuation of slat trailing edge noise.

1. INTRODUCTION

For modern commercial airliners with high bypass ratio turbofan engines, airframe noise has emerged as a leading component of the overall aircraft noise during the final

approach-to-landing phase. With the growth of traffic, the annoyance near airports is increasing and the environmental concerns and noise certification regulations make the study of airframe noise an important research topic.

Some earlier tests have identified leading edge slat noise as a dominant component of the total airframe noise during approach[1, 2, 3]. In general, the slat noise acoustic spectrum contains both high frequency tonal components and broadband components covering the lower and mid frequencies[2,4]. Generally, for a commercial aircraft in flight, the broadband noise is more important since the A-weighted spectrum peaks at around 800Hz[5]. Recent experiments and numerical simulations have suggested that the high frequency tonal noise radiates from a region in the vicinity of the slat trailing edge[6, 7]. The source of the broadband noise is less clear however. It is has been shown to be associated with the unsteady flow in the slat cove region[8, 9, 10], but others have suggested that the actual noise source is located at the slat trailing edge, and that the source is due to the convection of the turbulence past that edge[5, 11].

Lighthill demonstrated that aerodynamic noise is caused by shear stresses distributed through the fluid[12]. In jet noise, where the sources radiate independently of solid surfaces, the sources are relatively inefficient and obey an M^8 power law. When the source is associated with flow over a bluff body, such as an aircraft landing gear, the noise obeys an M^6 power law[13]. However, noise radiated by turbulence convected past a trailing edge is a more efficient source of aerodynamic noise, and Ffowcs Williams and Hall demonstrated that the scattering effect of the trailing edge increases the efficiency of the source to an M^5 power law[14]. The fact that slat noise measured for aircraft in flight obeys an M^5 power law[15] is a key point in favour of the slat trailing edge being the dominant source of noise radiation, although this says nothing about the origins of the turbulence that drives the source.

The importance of slat noise as a source of community noise disturbance is partly a function of its directivity, with slat noise tending to dominate when the aircraft is in the overhead position, when the aircraft is at its point of closest approach to an observer. It has been argued that this directivity may be associated with the acoustic characteristics of the slat gap, with the local geometry and flow combining to increase further the acoustic efficiency of the trailing edge source and to redirect the sound towards the ground, as illustrated in Figure 1[5].

Besides being dependent on the slat gap geometry, the directivity of slat trailing edge noise will also be a function of the directivity of the source. For a compact aerofoil, such as a helicopter blade, Amiet showed that the trailing edge source would have a dipole-like $\sin^2(\theta_T)$ directivity[16], whereas Ffowcs Williams and Hall showed that for a semi-infinite plate the directivity would be a $\sin^2(\theta_T/2)$ cardioid shape[14]. Here θ_T is the angle relative to the trailing edge as show in Figure 1. At 800 Hz the slat chord is comparable with the wavelength of the sound and so the directivity of the source and its radiation characteristics into the slat gap is likely to be a complex function of frequency, flow and slat geometry. These complexities create problems for experimentation at model scale since the turbulence that drives the aerodynamic noise source scales differently from the acoustic radiation characteristics into the slat gap; this provides a good reason for developing some understanding of the problem through the use of numerical models.

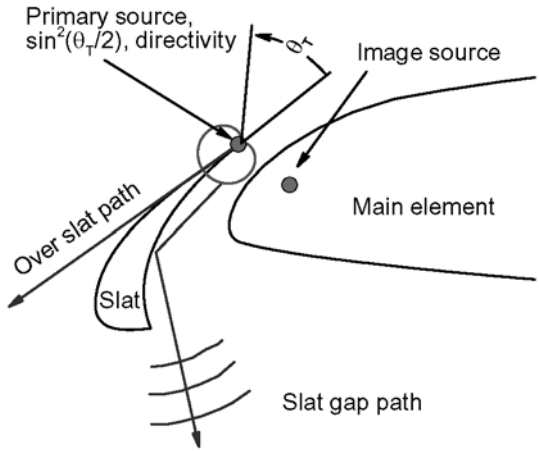

Figure 1. Notional acoustic model for slat noise trailing edge source directivity.

If the slat trailing edge is ultimately identified as the dominant location for broadband noise generation, then the notional model shown in Figure 1 may be used to show why using acoustic liners in the slat gap region might provide useful attenuation; absorptive treatment on the surface of the main element would suppress the image source and treatment in the slat gap would attenuate the sound as it propagates away from the source. This potential benefit of such treatment has been investigated in experiments by Smith *et al*[17]. Unlike other noise control techniques, such as serrated tape at the slat trailing edge or slat cove fillers, the acoustic liner treatment would not modify the slat shape and would thus be expected to have minimal effect on the wing pressure distributions and the resulting lift. An exception to this would be treatment on the highlight of the main wing element, which might provide useful attenuation by influencing the diffraction around the wing, but might also be expected to have an aerodynamic penalty by modifying the local flow.

The objective of the present research therefore, is to use a numerical model to explore the concept of attenuating slat trailing edge noise using acoustic liners in the slat gap, taking into account the local flow characteristics. The acoustic liner should attenuate both the broadband noise and the tonal noise but, because methods for predicting numerically the generation of broadband noise are still being developed, the results presented here concentrate on the attenuation of the high frequency tonal components.

Traditionally, the impedance condition required to model acoustic liners has been limited to frequency domain computational methods, primarily because of the frequency dependent characteristics of liner materials. Time domain applications of such materials are difficult to simulate because of computationally expensive convolutions in the calculations. Time-domain methods are easy to apply within large computational fluid dynamics (CFD) calculations however, which makes the coupled computation of aeroacoustics and aerodynamics possible. Recently Fung *et al*. proposed a method for the derivation of a stable time-domain impedance boundary

condition (TDIBC) from the reflection coefficient, rather than using the impedance as is ordinarily done[18]. This method has now been implemented in the high-order CFD code at Southampton University so as to investigate the slat gap liner concept.

The computational work is divided into three parts: (1) an URANS simulation using high-order spatial and temporal schemes is conducted for a wing with high-lift devices deployed without acoustic liner; the computed flow shows the presence of vortex shedding and acoustic sources behind the slat trailing edge; (2) a calculation of the radiated sound field is made for a range of liner impedance values by solving the linearised Euler equations with a representation of the computed acoustic source at the trailing edge of the slat; (3) URANS computations with acoustic liner treatments are conducted for the case of a liner on the slat cove and for a combination of a liner on the slat cove surface and a liner on the main element.

The organization of the paper is as follows. The numerical method used in the simulations are described in the section 2, in which the spatial discretization algorithm, time advancing method and time domain impedance boundary condition etc. are presented in detail. In Section 3 computational results are presented and analyzed. For both the nonlinear viscous case and the linearised inviscid case, the acoustic field without and with the liner treatment on the slat and the main element are calculated and compared. Unless indicated otherwise, all calculated results are shown in International System of Units (SI) system. Finally conclusions are given in Section 4.

2. NUMERICAL METHODS

2.1 Governing equations

The viscous flow field over a high-lift device is calculated by solving the two-dimensional time-dependent compressible Reynolds averaged Navier-Stokes equations,

$$\frac{\partial \hat{Q}}{\partial t}+\frac{\partial \hat{F}}{\partial \xi}+\frac{\partial \hat{G}}{\partial \eta}=\frac{1}{\mathrm{Re}}\left[\frac{\partial \hat{F}_v}{\partial \xi}+\frac{\partial \hat{G}_v}{\partial \eta}\right] \tag{1}$$

where $\hat{Q}=(1/J)[\rho, \rho u, \rho v, \rho E]^T$ denotes the solution vector and $J=\partial(\xi, \eta)/\partial(x, y)$ is the transformation Jacobian. $\hat{F}, \hat{G}$ are the inviscid fluxes and $\hat{F}_v, \hat{G}_v$ are the viscous fluxes[19]. Here (x, y) are the Cartesian coordinates and (ξ, η) are the generalized coordinates; $(\rho, \rho u, \rho v, \rho E)$ are density, velocity component in the x direction, velocity component in the y direction, and total energy per unit mass respectively; t is time; Re is Reynolds number.

The Spalart-Allmaras (S-A) model[20] used in this study solves a single field equation for a variable $\hat{v}$ related to the eddy viscosity. Although an earlier study[6] has shown that full turbulence calculations have excessive diffusive effects, especially for the slat cove flow, the present calculation work assumes fully turbulent flow over the wing and focuses on the vortex shedding induced high frequency tonal noise emanating from the vicinity of the slat trailing edge.

For the acoustic liner prediction model, the governing equations are the two-dimensional linearised Euler equations,

$$\frac{\partial}{\partial t}\begin{bmatrix} u' \\ v' \\ p' \end{bmatrix} + \frac{\partial}{\partial x}\begin{bmatrix} p' \\ 0 \\ u' \end{bmatrix} + \frac{\partial}{\partial y}\begin{bmatrix} 0 \\ p' \\ v' \end{bmatrix} = 0 \tag{2}$$

where (u', v', p') are velocity perturbation in the x direction, velocity perturbation in the y direction and pressure perturbation respectively. It should be noted that the continuity equation has been dropped since it is essentially the same as the energy equation.

2.2 Spatial discretization

For a given scalar quantity ϕ, the first spatial derivative $(\partial\phi/\partial\xi)_i$ at any point i is computed in the transformed plane by solving the following system of equations:

$$\frac{1}{2}D_i^F = \frac{1}{2\beta_F\Delta\xi}[b_F(\phi_{i+1}-\phi_i)+d_F(\phi_{i-1}-\phi_i)+e_F(\phi_{i-2}-\phi_i)]-\frac{\alpha_F}{2\beta_F}D_{i+1}^F \tag{3}$$

$$\frac{1}{2}D_i^B = \frac{1}{2\beta_B\Delta\xi}[b_F(\phi_i-\phi_{i-1})+d_F(\phi_i-\phi_{i+1})+e_F(\phi_i-\phi_{i+2})]-\frac{\gamma_B}{2\beta_B}D_{i-1}^B \tag{4}$$

$$D_i = \frac{1}{2}(D_i^F + D_i^B) \tag{5}$$

where D_i, the desired approximation of the spatial derivative, is obtained by adding the forward D_i^F and backward D_i^B estimates of the spatial derivative. The coefficients $b_F, d_F, \ldots$, determine the spatial properties of the algorithm. The systems of equations encompass a family of schemes ranging in accuracy from the standard three-point, second-order accurate explicit method to a compact seven-point, eighth-order algorithm. In this work a fourth-order compact scheme[21] is employed to evaluate the spatial derivatives.

The algorithm is first used to construct various metrics, $\partial x/\partial\xi$, $\partial x/\partial\eta$,…, which in turn are used to calculate the transformation Jacobian J. The inverse metrics,$\partial\xi/\partial x$, $\partial\xi/\partial y$,… are then obtained using the standard general transformation relationships. The derivatives of the inviscid fluxes are obtained by first forming the fluxes at the nodes and then differentiating each component using the above formulae. For the computation of the viscous terms, the primitive variables, u, v, w and T are first differentiated to form the components of the stress tensor and the heat flux vector at each node. The viscous flux derivatives are then computed by a second application of the same scheme.

2.3 Temporal integration

For the viscous flow calculation, a fourth order Runge-Kutta method[22] is used to advance the solution in time. For the acoustic liner optimization calculation, the explicit low-storage Runge-Kutta scheme due to Hu, *et al*.[23] is used. This is an optimized two-step alternating scheme, in which different coefficients are employed in the alternating steps. To lower the computational overheads the two-step alternating scheme is implemented in a low storage format. The implementation requires three levels of data storage, as opposed to four levels for the classical fourth-order Runge-Kutta scheme.

2.4 Filter scheme

The prefactored compact scheme used is the centered scheme, and therefore contains no inherent dissipation. Whilst this is desirable for wave propagation, it does make such schemes susceptible to failure from the unchecked growth of high-frequency modes. Such modes can originate from mesh non-uniformity, boundary conditions, non-linear flow features, or poorly specified initial conditions. To overcome these difficulties, and to extend the flow solver to the complex slat flow computation, whilst retaining the improved accuracy of the spatial compact discretization, a high-order implicit filter technique[24] has been incorporated.

If a component of the solution vector is denoted by ϕ, filtered values $\hat{\phi}$ are obtained by solving the tridiagonal system

$$\alpha_f \hat{\phi}_{i-1} + \hat{\phi}_i + \alpha_f \hat{\phi}_{i+1} = \sum_{n=0}^{N} \frac{a_n}{2} (\phi_{i+n} + \phi_{i-n}), \tag{6}$$

where the coefficients a_f, a_0, $a_1 \ldots a_N$ determine the order and spectral response of the filter. With a proper choice of these coefficients, Equation (6) provides a $2N$th-order formula on a $2N+1$ point stencil. Visbal and Gaitonde[24] showed, using a combination of Taylor- and Fourier-series analyses, that the $N+1$ coefficients a_0, $a_1 \ldots a_N$ could be expressed solely in terms of α_f. The adjustable parameter $\alpha_f \in (-0.5, 0.5)$ then determines the dissipative characteristics of the filter for a given degree of accuracy. For the work presented in this paper the eighth-order filter variant has been used, with $\alpha_f = 0.495$. This choice ensures the spectral characteristics of the filter closely match those of the spatial compact discretization, thus preserving accuracy.

The eighth-order formula requires a nine point stencil; it is therefore not suitable for use at or near boundary points. In these regions, the order of accuracy of the filter is reduced as the boundary is approached to the level for which a centered scheme is available. Values along the boundary points are left unfiltered. The filter is applied sequentially in each coordinate direction to the conserved variables at every timestep.

2.5 Buffer zone boundary condition

At present, solutions of the URANS equations, or even the linearised Euler equations, over large domains to determine far-field noise are not computationally feasible. A computational domain must be truncated by the introduction of artificial boundaries. Numerical non-reflecting boundary conditions are required at such boundaries to ensure that out-going disturbances are not reflected. An explicit damping buffer zone method[25] is used in this work. The computational grid is extended to create an extra layer, buffer zone, surrounding the main computational domain and in the buffer zone the solution vector is explicitly damped after each timestep using

$$Q^{n+1} = \bar{Q}^{n+1} - \sigma(\bar{Q}^{n+1} - Q_{target}), \tag{7}$$

where $\bar{Q}^{n+1}$ is the solution vector after timestep n and Q_{target} is the expected value in the buffer zone. The damping coefficient, σ, varies smoothly according to the function,

$$\sigma(x) = \sigma_{\max}\left|1 + \frac{x_b - L}{L}\right|^{\beta} \tag{8}$$

where L is the width of the buffer zone, x_b is the distance measured from the inner boundary of the buffer zone and $\sigma_{\max}$ and β are coefficients which determine the shape of the damping function. The $\sigma_{\max}$ decides the maximum value of damping coefficient and β decides the damping rate. The greater the value of β, the less damping applied. In the present study, $\sigma_{\max}$ =1.0 and β = 2.5 are used and the width of the buffer zone L is defined by a total of 20 grid points surrounding the URANS and LEE computational domains.

2.6 Time-domain impedance boundary condition

On the acoustically treated wall, the time domain impedance boundary condition proposed by Fung *et al*.[18] is applied. Let p' and u_n' be the time domain acoustic pressure and the normal particle velocity (positive when pointing into the surface) on the impedance wall nondimensionalized by the freestream sound speed c_0 and dynamic pressure $\rho_0 c_0^2$. Define $u_n'^{-} = u_n' - p'$ and $u_n'^{+} = u_n' + p'$. In the frequency domain the reflected wave $\hat{u}_n'^{-} = \hat{u}_n' - \hat{p}' = (1 - Z)\hat{u}_n'$ is related to the incident wave $\hat{u}_n'^{+} = \hat{u}_n' + \hat{p}' = (1 + Z)\hat{u}_n'$ by

$$\hat{u}_n'^{-} = \hat{W}(\omega)\hat{u}_n'^{+} \tag{9}$$

where $Z = \hat{p}'/\hat{u}_n'$ is the normalized impedance of the boundary; ω is frequency and $\hat{W}(\omega) = (1\text{-}Z)/(1+Z)$ is the reflection coefficient. The complex function $\hat{W}$ provides a direct measure of the magnitude of the reflected wave and its phase relative to the incident wave.

The frequency domain relationship is equivalent to the time domain convolution process:

$$u_n'^{-}(t) = \int_{-\infty}^{\infty} W(t-\tau)u_n'^{+}(\tau)d\tau \tag{10}$$

The evaluation of this convolution integral is computationally expensive and is therefore not suitable for practical computation. However, using a suitable impedance model can give a more computationally favorable reflection coefficient behavior. A three-parameter model is used which can be written as:

$$Z(\omega) = R + iX = R + i(X_{-1}/\omega + X_1\omega) \tag{11}$$

where R and X are the resistance and reactance of the liner which are nondimensionalized by the free air impedance $\rho_0 c_0$,where ρ_0 and c_0 are the freestream density and speed of sound. X_1 and X_{-1} are the acoustic mass and stiffness used to fit the liner reactance value. Using this model if X_1>0 and X_{-1}<0, then $W(t)$ is causal and can be confined in a finite time history. Beyond this finite time history, the reflection kernel is either zero, or insignificantly small. This implies that the expensive convolution can

be replaced by an integral sum. Using the recursive formula given in Ref. [26], the time domain impedance boundary condition can be implemented efficiently.

2.7 Details of the computation

For the URANS simulations, 1.16 second CPU time per timestep is needed based on eight 2.2 GHz AMD Opterons CPUS with 16 GB of RAM. After the initial transient phase, 2,000,000 steps are advanced for the hardwall case. The hardwall result is used as the initial condition for the lined wall cases and 680,000 steps are calculated for each lined wall case.

For the LEE computation, 0.9 second CPU time per timestep is required based on a 3.0 GHz Intel XEON CPU with 2 GB of RAM. Every case required 1 hour 42 minutes to complete and a total of 66 cases are assessed.

3. COMPUTATIONAL RESULTS

3.1 Aeroacoustic simulation with hardwall condition

A simulation of the viscous flow field without acoustic liner treatment is performed first to capture the pattern of the acoustic field induced by the flow over the slat of the standard hard wall high-lift wing. The wing model comprises a main element, a leading edge slat and a trailing edge flap geometry (Figure 2). The model has a chord length C of 0.8m without the slat and flap deployed. The slat and flap chords are 12% and 26% of the overall chord length, respectively. The main geometry settings are listed in Table 1, where the distances are given as percentages of the chord in the stowed configuration and the angles are the relative angles of the stowed position and the deployed position. The freestream Mach number is 0.2 and the main element angle of attack is 5 deg, corresponding to a typical approach condition. The Reynolds number is 3.6 million, based on the airfoil chord with the high-lift devices retracted.

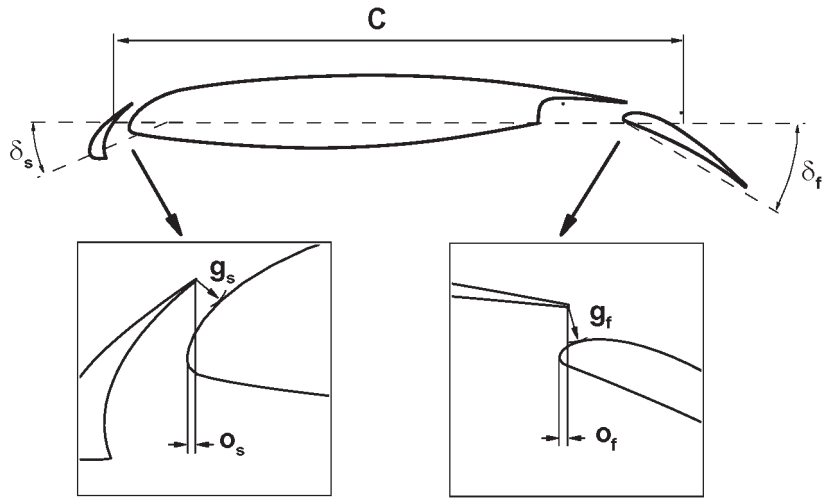

Figure 2. Geometry of three-element wing model.

Table 1. Geometrical settings for high-lift devices

Parameter	Setting
Slat angle δ_s, deg	23
Slat gap g_s, %	1.7
Slat overhang o_s, %	0.5
Flap angle δ_f, deg	32
Flap gap g_f, %	2.0
Flap overhang o_f, %	0.55

For this high-lift flow computation the grid must be handled with care so that accurate results are obtained with an acceptable number of grid points. In our computation, mesh clustering is enforced near solid surfaces, around the trailing edge of the slat, in the wake behind the slat, and around the cove of the slat as shown in Figure 3. The 1-1 matched grid block topology is used to achieve the necessary high accuracy. The two-dimensional grids have 34 zones, with a total of 393,574 grid points and with nearly a quarter of the points clustered in the vicinity of the slat. In order to capture the vortex shedding near the trailing-edge, the tailing edge of the slat had a thickness *h* of 0.59 mm rather than an idealized sharp edge (Figure 4) and 49 grid points are used across the thickness of the slat trailing edge.

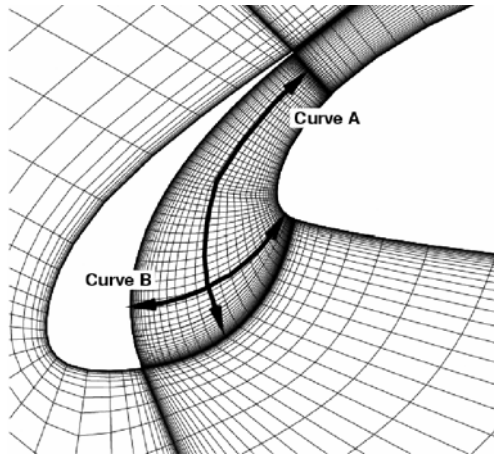

Figure 3. A view of the grid in the vicinity of the slat. Every 4th point is shown.

The time-accurate solution is quasi-periodic after the initial transient phase. The time-averaged Mach contours near the slat (Figure 5) display a recirculation zone in the slat cove, a shear layer originating from the slat cusp and acceleration of the local flow through the gap. In Figure 5 a shear layer is seen to separate the gap flow and the recirculation zone. The shear layer thickens as it curves up and reattaches to the cove surface near the slat trailing edge. The shear layer is a good amplifier of the

unsteadiness generated near the cusp of the slat. In fact features such as shear layer instabilities and roll-up of large vortical structures were reported in earlier model tests[10, 27]. Due to the excessive dissipative effect of the turbulence model the present simulations fail to capture these phenomena. Figure 6 shows an instantaneous vorticity field near the slat cove region, where vorticity is defined as the curl of the velocity vector. In the slat cove region the vorticity field is nearly stable and no large scale coherent structures are captured in the current URANS simulations.

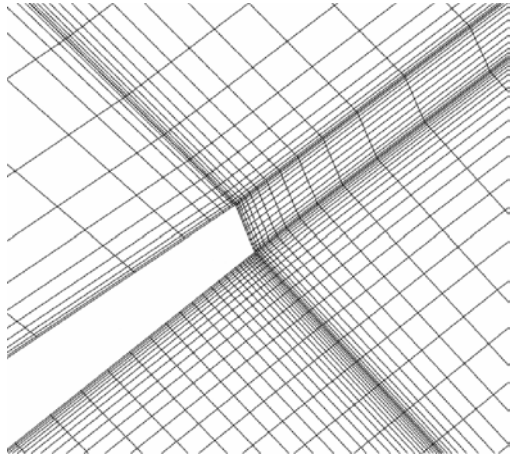

Figure 4. A view of the gird near the trailing edge of the slat. Every 4th point is shown.

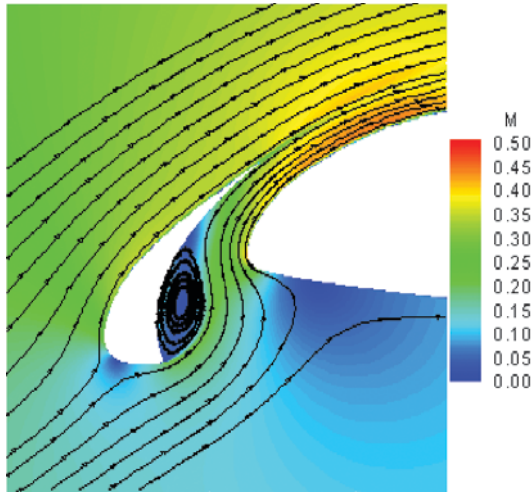

Figure 5. Time-averaged Mach contours.

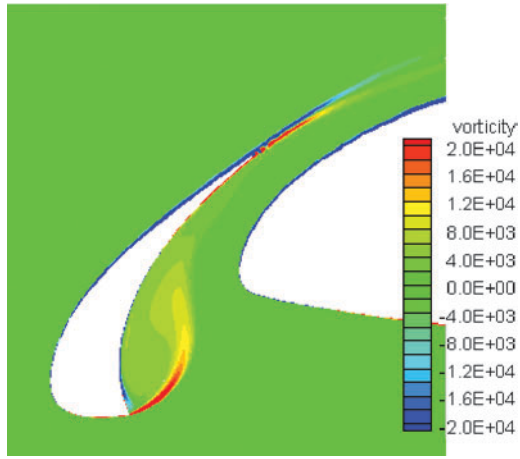

Figure 6. Instantaneous vorticity contours.

Periodic flow fluctuations are mainly concentrated at the slat trailing edge, and are caused by the vortex shedding at that edge because of the global wake instability[28, 29]. A region of absolute instability of sufficient length and growth rate existing in the near-wake of a body is a necessary condition for the existence of vortex shedding. In Figure 7, the time-averaged Mach contours near the slat trailing edge show some characteristics of the trailing edge wake. Because the flow through the gap moves faster, the wake is asymmetric and exhibits an upward deflection. Close to the edge, the wake possesses a region of reversed flow. This region suggests the existence of absolute instabilities which cause the vortex shedding phenomenon. The instantaneous vorticity field behind the slat trailing edge is shown in Figure 8. The established vortex street shows the existence of vortex shedding at the trailing edge.

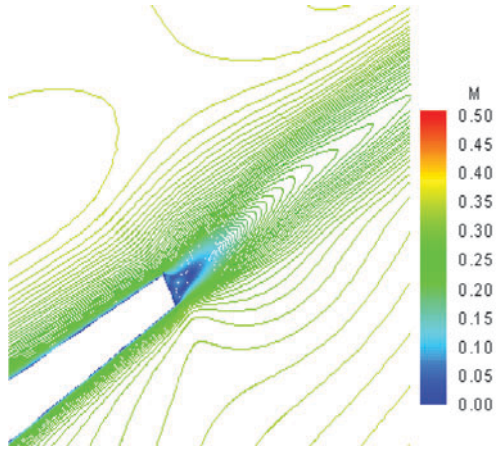

Figure 7. Time-averaged Mach contours near the trailing edge of the slat.

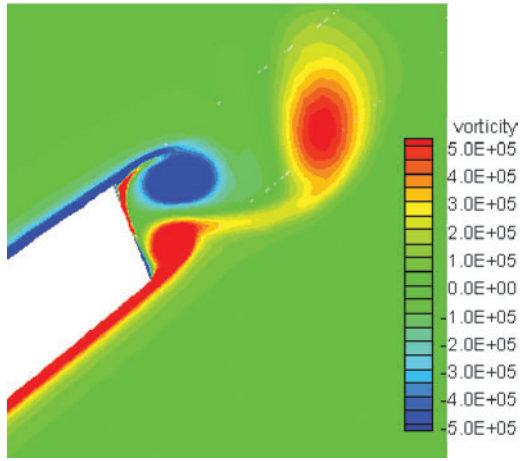

Figure 8. Instantaneous vorticity field near the trailing edge of the slat.

Figure 9 shows acoustic waves and established wave patterns near the trailing edge and cove region of the slat. The fluctuating field is obtained by subtracting the local mean value from the total unsteady solutions. The acoustic waves are seen to emanate from the trailing edge and impinge on the surface of main element. The waves are reflected, as depicted by the image acoustic source in Figure 1. As the waves propagate downward along the slat cove and main element surface there is a distinct interference pattern across the gap and in the cove area, which is indicative of modal propagation in the slat gap and as illustrated by the reflected ray path in Figure 1. The sound is channeled down the slowly expanding channel of the slat gap and is diffracted around the edge of the main element and the cusp of the slat. It is directed towards the ground when the aircraft attitude is taken into account.

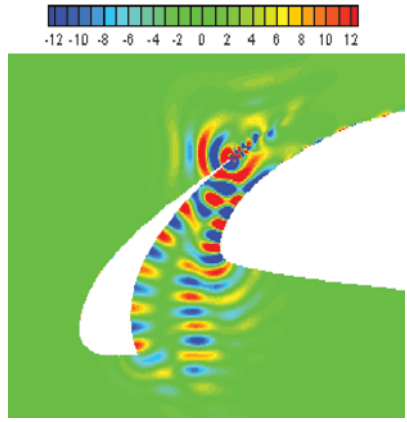

Figure 9. Fluctuating pressure field around the slat.

The frequency spectrum of the pressure fluctuations near the slat trailing edge is shown in Figure 10. The pressure monitoring point is located along the slat chord line at a distance of 1.18 mm from the trailing edge of the slat. The spectrum is obtained by performing a fast Fourier transform (FFT) of the monitored pressure history. The sampling rate is 4.25×10^7 and a total of 55,400 samples are used corresponding to 32 periods of oscillation of the vortex shedding frequency. The resulting frequency resolution is about 760 Hz. Figure 10 shows that the self-excited hydrodynamic resonance - vortex shedding - produces sharp peaks in the spectrum at harmonics of the fundamental vortex shedding frequency of 25 kHz. There are elements of broadband noise but it should be noted that the URANS simulation is likely to suppress the broadband noise component.

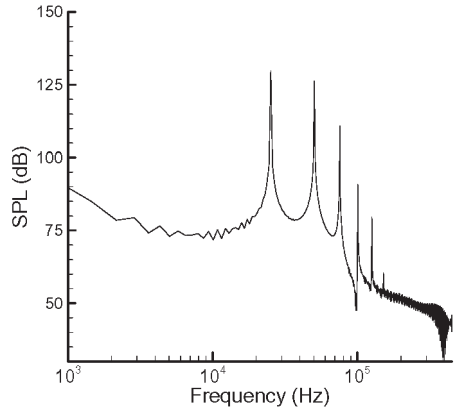

Figure 10. Pressure spectrum near the trailing edge of the slat.

A refined-grid aeroacoustic calculation with hardwall condition was performed to test the accuracy obtained in the preceding results. The details of the grids are given in Table 2; Grid 2 is the grid used in earlier calculation. The Fourier transform of the monitored pressure history shows that the shedding frequency is 24 kHz for the refined-grid calculation. The SPL at the monitor point is 127dB for the refined-grid solution and 129 dB for the original-grid solution. The small difference in amplitude and frequency of the monitored pressure reveals that the results of original computation have little grid dependency and their accuracy is verified sufficiently.

Table 2. Grid distributions near the trailing edge slat

	Grid 1	**Grid 2**
Grid points along curve A	401	353
Grid points along curve B	257	197
Grid points along slat trailing edge	65	49

*Curve A and curve B are shown in Figure 3

3.2 Liner impedance optimization

The URANS can predict the noise source more accurately, but it is very time consuming and not suitable for an optimization process for the impedance of the acoustic liner. This part of liner impedance optimization study is conducted by solving the linearized Euler equations with the assumption of zero mean flow.

Based on the viscous flow result, the source of noise near the trailing edge is modelled with a 25 kHz dipole. The dipole is realized by adding a source term to the energy equation of the LEE that can be written as:

$$q = A_m \cdot \sin(\omega t) \cdot \exp\left(-\ln(2)\frac{(x-x_1)^2+(y-y_1)^2}{b^2}\right) - A_m \cdot \sin(\omega t) \cdot \exp\left(-\ln(2)\frac{(x-x_2)^2+(y-y_2)^2}{b^2}\right) \quad (12)$$

with ω=462; A_m=0.0025 ω and b=0.005. (x_1, y_1) and (x_2, y_2) are given as (–0.00015, 0.00018) and (0.00015, –0.00018) respectively.

The computational grid used for the slat gap LEE liner study is shown in Figure 11. A total of 87,498 grid points are used and the maximum grid size is 1.0×10^{-3} m, which gives an equivalent grid resolution of at least 12PPW (points per wavelength) for frequencies up to 25 kHz. In the LEE modelling process, the trailing edge of the slat is treated as a sharp edge, rather than the blunt edge used in the viscous calculation, in order to avoid the need for a fine grid near the trailing edge of the slat.

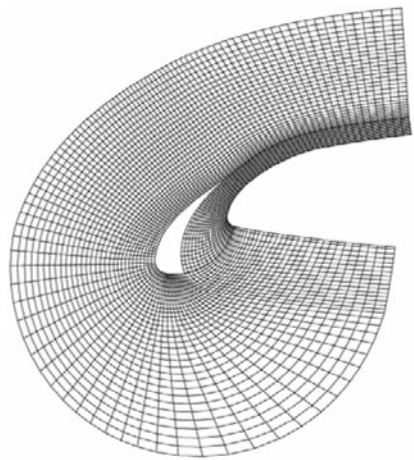

Figure 11. Computational grid for liner evaluation. Every 4th point is shown.

The liner condition is applied to the slat cove surface and part of main element surface as shown in Figure 12. The slat cove liner starts from the cusp of the slat, but at the slat trailing edge the available depth is too small to apply a practical liner, the liner

treatment is thus only extended to a position where at least 5 mm depth is available. The liner length is 76% of the total slat cove surface length. On the basis that the acoustic liner on the main element should probably avoid the leading edge stagnation point, so as to minimize any possible aerodynamic penalty, the liner starts from a position on the suction surface at a distance of $0.01C$ from the leading edge and is extended for a distance of about six wavelengths at the source frequency; numerical tests show that any further extension of the liner treatment would have an insignificant effect on the noise attenuation performance.

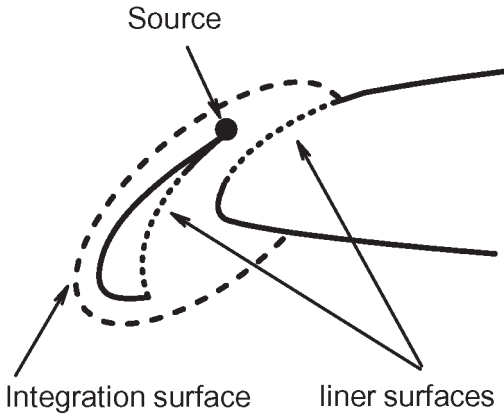

Figure 12. A schematic of the LEE liner study.

To provide an assessment of the benefit of the acoustic liners, the farfield directivity is obtained by solving Ffowcs Williams-Hawkings (FW-H) equations using formulation 1A of Farassat[30], in which the volume quadrupole terms are neglected. The integration surface for solving the FW-H equation is generated by extruding a curve in the spanwise direction with a span from -0.5m to 0.5m and the end (lateral) surfaces are not included in the integration. Setting the trailing edge of the slat as the origin, the curve is a portion of an ellipse which is generated by rotating the ellipse anti-clockwise by 40 deg and the ellipse is centered at (-0.0068, -0.0322) with a major axis of 0.0774 m and a minor axis of 0.0372 m. The integration surface is truncated by the main element. The data along the integration surface are obtained by performing a bilinear interpolation using the nearest four grid points. The farfield observers are positioned at z=0 plane on a circle with a radius of 12.5C from the trailing edge of the slat.

The objective function for the evaluation process needs to show the change in the acoustic field of the wing between the hardwall case and the lined wall as a function of the liner resistance R and reactance X; it is assumed here that the same impedance will be used on both the slat cove liner and the main wing liner. The objective function for liner optimization can be written as:

$$A = 10\log_{10}\left(\int_{s_0}^{s_1} \left|p'_{rms}\right|^2_{hard}\, ds \Big/ \int_{s_0}^{s_1} \left|p'_{rms}\right|^2_{lined}\, ds\right), \tag{13}$$

where A stands for the space averaged attenuation, $|p'_{rms}|_{hard}$ is the root mean square (RMS) acoustic pressure for the hardwall case and $|p'_{rms}|_{hard}$ is the RMS acoustic pressure for the lined wall case. S denotes the distance measured along the observer circle. As the noise propagating towards the ground is mostly concerned, the attenuation is evaluated on a truncated portion of the observer circle between the observation angles of 240 deg and 340 deg. The angle here is relative to the positive x direction and increases anti-clockwise. The position of the acoustic source, the integration surface around the slat and the location of the acoustic liners are shown in Figure 12.

The contours of attenuation are plotted in the impedance plane to obtain the maximum of the objective function (Figure 13). A 6×11 grid in the design variable space (resistance, reactance) is used so that a total of 66 cases are assessed. The results are shown in Figure 13; there are well-defined optimum points: R=1.1 X=–2.0. The relatively large region of the impedance plane over which optimal or near optimal liner behavior is predicted suggests that a liner designed with no mean flow should also perform well for the case with a mean flow up to perhaps Mach number 0.3[31], although the negative mean flow (sound propagating upstream) may be expected to increase the attenuation slightly, and may result in a slightly different optimum impedance value.

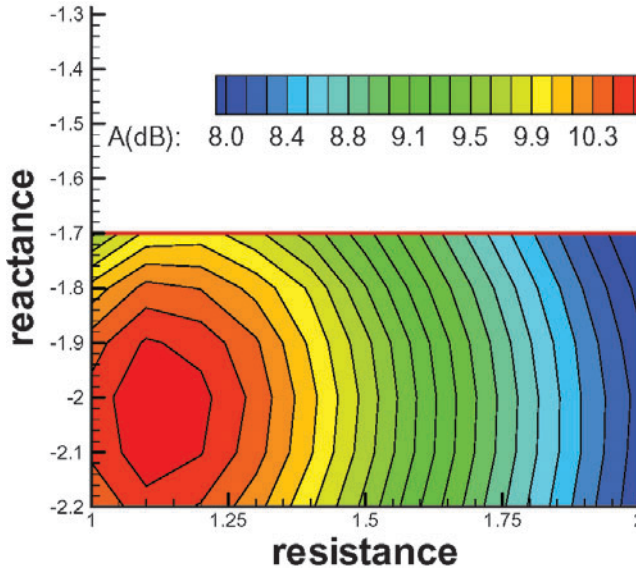

Figure 13. Attenuation contour map.

The effect of the liner arrangement is now considered. The instantaneous acoustic pressure contours for four different cases (hard-wall, lined slat, lined main wing and both slat and wing liners) are shown in Figure 14. The liner positions are highlighted by the solid black lines in each figure. The characteristics of the acoustic field at 25 kHz with and without the liners can be seen clearly.

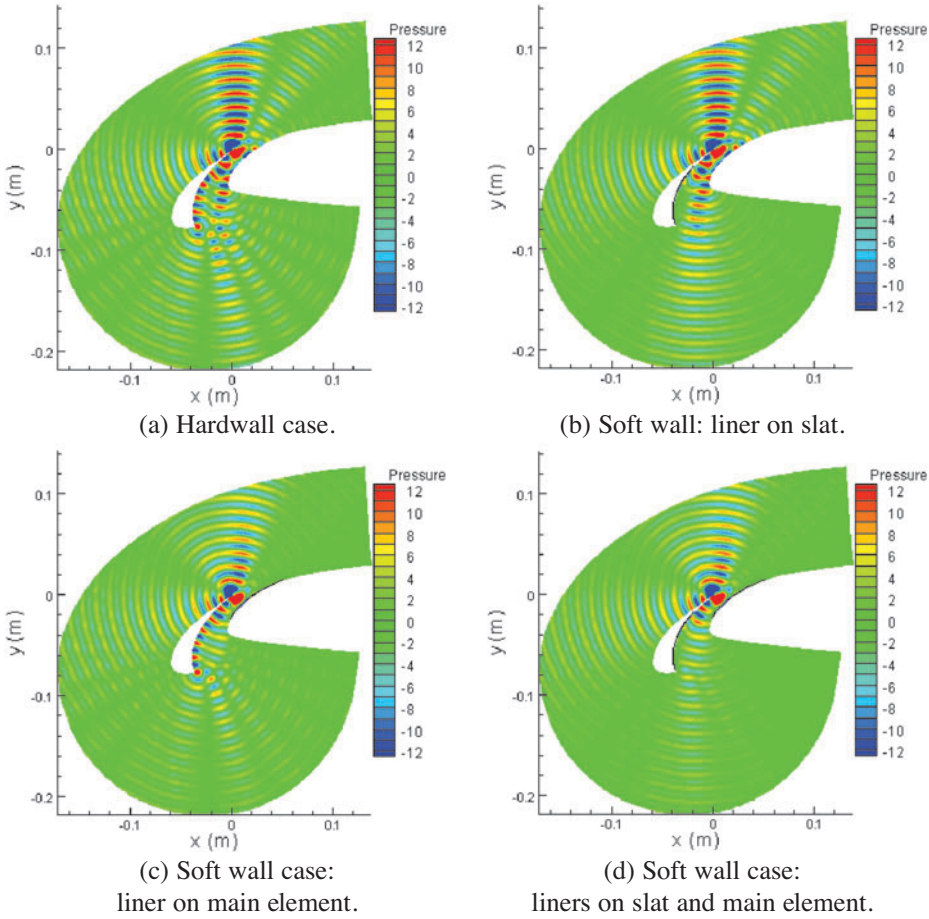

(a) Hardwall case.

(b) Soft wall: liner on slat.

(c) Soft wall case: liner on main element.

(d) Soft wall case: liners on slat and main element.

Figure 14. Contours of acoustic pressure.

Figure 15 shows the farfield directivity for the different liner arrangements considered. In Figure 15(a) the complete directivity plot is shown, with the distance of the line from the origin at any angle being proportional to the integrated RMS pressure that radiates in that direction; the x direction in Figure 14 is defined as θ=0 deg, with the angle increasing anti-clockwise. In Figure 15(b) the important angles radiating through the slat gap are shown as a decibel level.

In Figure 15 the black line represents the directivity for the hardwall case; there are large radiation peaks in the upward direction and smaller peaks in the forward direction as well as the downward direction through the slat gap. As might be expected, the presence of the main element blocks downstream radiated noise. It should be noted however that the details of this radiated sound field does not agree with the pressure field shown in Figure 9, where the predominant noise radiation is through the slat gap. This suggests that the dipole source used in the acoustic predictions may not be fully representative of the actual aerodynamic source.

The other lines in Fig 15 show the directivity for the acoustically lined cases. In each case there is some effect in reducing noise radiation upwards, although the effect in this direction is small for the slat cove liner. The liners produce little effect in the radiated noise in the upstream direction. As might be expected however, the main effect of the liners is a large reduction in noise radiation at angles from 240 to 340 deg where the sound has propagated through the slat gap. Generally there are good attenuations for the wave radiated through the slat gap in the 240 to 320 deg range. The slat cove liner is predicted to cause a small increase in noise radiation in the 255 to 275 deg range. The combined effect of slat liner and main element liner, shown by the red line, gives the largest reduction. It should be noted that the combined liner arrangement enables a shift in the radiation peaks.

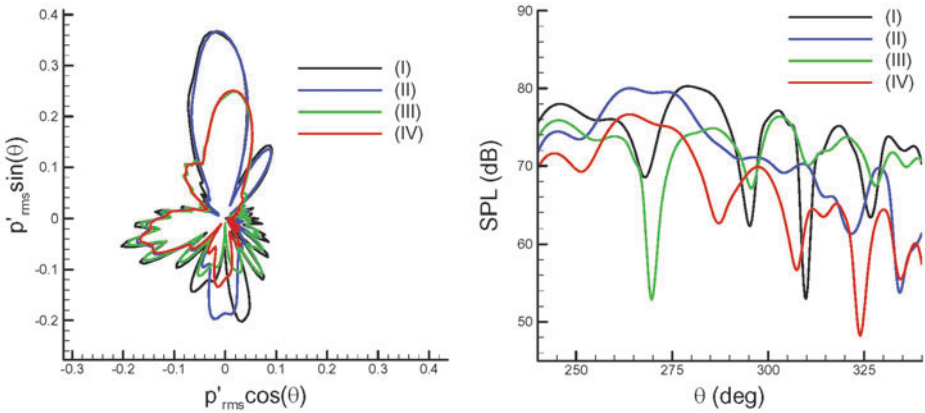

(a) Complete directivity (b) Partial directivity

Figure 15. Directivity of acoustic pressure for different liner arrangement: (I) hardwall, (II) lined slat, (III) lined main element, and (IV) liners on slat and main element.

3.3 Aeroacoustic simulation with lined walls

The linearised optimization study, using an idealized source in a no-flow condition, is clearly an approximation to the true situation although it is expected that the optimum impedance found will also be near optimum for the with-flow case. A fully viscous flow simulation for the three-element wing with the liner impedance boundary condition is now performed. The simulation employs the same free flow condition and the same high-lift device configuration as described in section 3.1 for the hardwall computation (see Figure 2).

The lined cases presented here are for a) the slat cove lined alone and b) both the slat cove and the main wing lined. Figure 16 shows the instantaneous fluctuating pressures around the slat. The solid black lines indicate the positions where the liner acoustic treatment is applied. Compared with the result of the hardwall case shown in Figure 9, both lined cases show significant attenuation of the sound field.

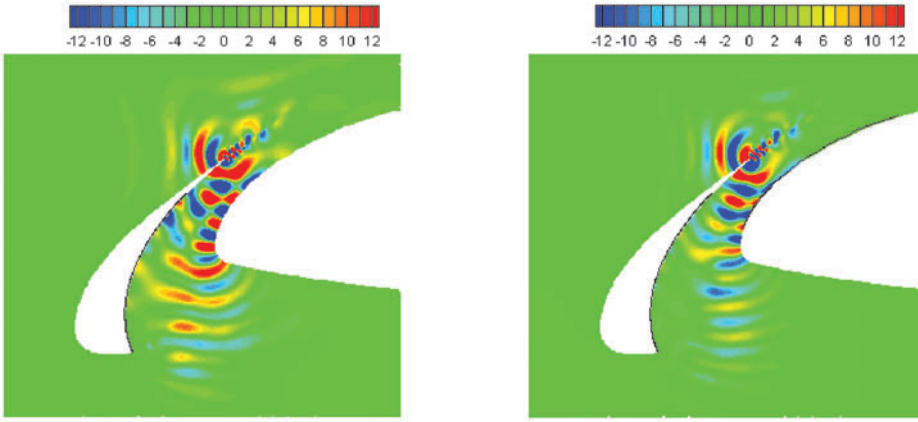

(a) (b)

Figure 16. Fluctuating pressure field near the leading edge; (a) liner on slat cove surface (b) liners on both slat cove surface and main element surface. Black solid line is the acoustic liner.

FW-H calculations are also performed to obtain the far field directivity. Figure 17 illustrates the integration surface used for the FW-H calculation; the solid line corresponds to the wing surface and the dashed line corresponds to the integration surface. The position of the integration surface must be handled with care to include all the major noise sources in the flow and it should be in the region where grid is fine enough to capture the acoustic signal without unacceptable dissipation. In the calculation, the integration surface used is a permeable surface that includes the boundary layers and vortex shedding region with a span from -0.5m to 0.5m in spanwise direction and the end (lateral) surfaces are not included in the integration. The off-body integration surface near the main element is located near the outer edge of the boundary layer and is extended for a distance of 0.2 C from the leading edge of the main element. Further extension of the integration surface along main element has an insignificant effect on the calculated FW-H results. As before, the observer points are positioned at z=0 plane on a circle with a radius of 12.5C from the upper point of the trailing edge of the slat. The farfield directivity patterns are shown in Figure 18. In Figure 18(a) the complete directivity patterns are shown. For the hardwall case, there are three peaks: upstream, upward and downward. The upward lobe is much smaller than that of LEE case with the dipole source. After the application of the acoustic liner, the upward peak and downward peak are attenuated significantly whilst in the upstream direction the directivity pattern shows insignificant changes. The directivity patterns in the angular range 240 deg to 340 deg are shown in Figure 18 (b). In this range the attenuation with a liner only on slat cove surface is 1.6 dB, whereas the attenuation with liners on both the slat cove and the main element is 4.1 dB. This indicates that the liner on main element has important contribution to the total attenuation.

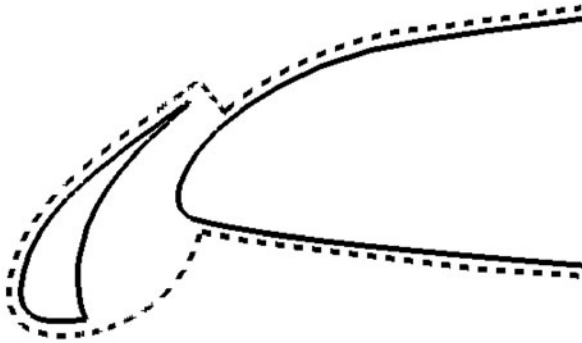

Figure 17. Integration surface used for FW-H calculations; black solid line is the wing surface and the red dashed line is the integration surface.

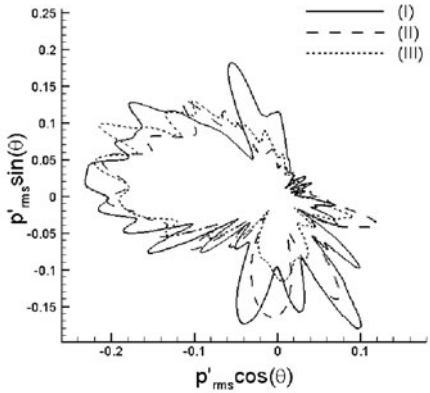

(a) Complete directivity

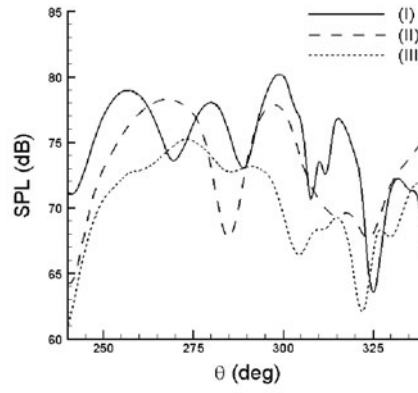

(b) Partial directivity

Figure 18. Directivity of acoustic signals for different liner arrangement: (I) hardwall, (II) lined slat, and (III) liners on slat and main element.

4. CONCLUSION

The concept of attenuating radiated slat noise using acoustic liners in the slat gap has been explored using a variety of numerical simulation methods. The computation of the fully turbulent flow field of the high-lift wing, which is simulated using a high-order numerical scheme, shows the expected vortex shedding from the blunt trailing edge and associated high-frequency tonal noise. The numerical model includes the modelling of absorptive liner material in the time domain using a time dependent impedance boundary condition. Linearised Euler computations are performed to evaluate a range of liner impedance values in the absence of flow using an idealized noise source near the trailing edge of the slat in order to identify an approximate optimum liner impedance. The flow field of the wing is simulated with the time dependent impedance boundary conditions on both the slat cove surface and suction surface of the main

element. The results show that liners on the slat and main element provide useful attenuation of slat noise.

Models of broadband slat noise sources, for example shear layer instability, formation of large scale coherent structures and shear layer-surface interaction are currently under investigation. The effectiveness of slat gap acoustic liners for these broadband sources will then be tested.

ACKNOWLEDGMENTS

Zhaokai Ma is supported by a studentship from the School of Engineering Sciences, University of Southampton, UK. The authors wish to thank Airbus for their funding support with Dr. L.C. Chow as industrial liaison of the project.

REFERENCES

1. Guo, Y. P., Yamamoto, K. J. and Stoker, R. W., "Component-Based Empirical Model for High-Lift System Noise Prediction," *AIAA Journal of Aircraft*, Vol. 40, No. 5, 2003, pp. 914-922.
2. Choudhari, M., Lockard, D. P., Macaraeg, M. G., Singer, B. A., Streett, C. L., Neubert, G. R., Stoker, R. W., Underbrink, J. R., Berkman, M. E., Khorrami, M. R. and Sadowski, S.S., "Aeroacoustic Experiments in the Langley Low-Turbulence Pressure Tunnel," NASA TM-211432, 2002.
3. Chow, L. C., Mau, K. and Remy, H., "Landing Gear and High Lift Devices Airframe Noise Research," AIAA Paper 2002-2408, 2002.
4. Dobrzynski, W., Nagakura, K., Gehlhar, B., and Buschbaum, A., "Airframe Noise Studies on Wings with Deployed High-Lift Devices," AIAA Paper 98-2337, 1998.
5. Smith, M.G. and Chow L.C. "Aerodynamic Noise Sources on High Lift Slats and Flaps," AIAA Paper 2003-3226, 2003.
6. Khorrami, M. R., Berkman, M. E. and Choudhari, M., "Unsteady Flow Computations of a Slat with a Blunt Trailing Edge," *AIAA Journal*, Vol. 38, No. 11, 2000, pp. 2050-2058.
7. Singer, B. A., Lockard, D. P., and Brentner, K. S., "Computational Aeroacoustic Analysis of Slat Trailing-Edge Flow," *AIAA Journal*, Vol. 38, No. 9, 2000, pp. 1558-1564.
8. Khorrami, M. R., Singer, B. A. and Berkman, M. E., "Time-Accurate Simulations and Acoustic Ananlysis of Slat Free-shear Layer," *AIAA Journal*, Vol. 40, No. 7, 2002, pp. 1281-1291.
9. Paschal, K., Jenkins, L. and Yao, C., "Unsteady Slat-Wake Characteristics of a High-Lift Configuration," AIAA Paper 2000-0139, 2000.
10. Takeda, K., Ashcroft, G. B. and Zhang, X., "Unsteady Aerodynamics of Slat Cove Flow in a High-Lift Device Configuration," AIAA Paper 2001-0706, 2001.
11. Dobrzynski, W. and Herr, M., "Experimental Investigations in Low Noise Trailing Edge Design," AIAA Paper 2004-2804, 2004.

12. Lighthill, M. J., "On Sound Generated Aerodynamically. II. Turbulence as a Source of Sound," *Proceedings of the Royal Society of London*, 222A, 1-32, 1954.
13. Curle, N., "The Influence of Solid Boundaries upon Aerodynamic Sound," *Proceedings of the Royal Society*, A231, 505-14, 1955.
14. Ffowcs-Williams, J.E., and Hall, L.H., "Aerodynamic Sound Generation by Turbulent Flow in the Vicinity of a Scattering Half Plane," *Journal of Fluid Mechanics*, Vol. 40, No. 4, pp. 657-70, 1970.
15. Molin, N., and Roger, M., "Use of Amiet's Methods in Predicting the Noise from 2D High Lift Devices," AIAA 2000-2064, 2000.
16. Amiet, R.K., "Noise Due to Turbulent Flow Past a Trailing Edge," *Journal of Sound and Vibration*, Vol. 47, 1976, pp. 387-393.
17. Smith, M.G., Chow L.C. and Molin N., "Attenuation of Slat Trailing Edge Noise using Slat Gap Acoustic Liners," AIAA paper 2006-2666, 2006.
18. Fung, K.-Y., Ju, H. B., and Talla Pragada, B., "Impedance and Its Time-Domain Extensions," *AIAA Journal*, Vol. 38, No. 1, 2000, pp. 30-38.
19. Anderson, D. A., Tannehill, J. C., and Pletcher, R. H., Computational Fluid Mechanics and Heat Transfer, 2nd ed., Taylor & Francis, Washington DC, 1997, pp. 250-257.
20. Spalart, P. R., and Allmaras, S. R. "A one-Equation Turbulence Model for Aerodynamic Flows," *LA Recherche Aérospatiale*, Vol. 1, 1994, pp. 5-21.
21. Ashcroft, G., Zhang, X., "Optimized Prefactored Compact Schemes," *Journal of Computational Physics*, Vol. 190, 2003, pp. 459-477.
22. Hirsch, C., *Numerical Computation of Internal and External Flows*, Volume 2, John Wiley & Sons, Chichester, 1990, pp. 334-337.
23. Hu, F. Q., Hussaini, Y. and Manthey, J., "Low-Dissipation and –Dispersion Runge-Kutta Schemes for Computational Acoustics," *Journal of Computation Physics*, Vol. 124, 1996, pp. 177-191.
24. Visbal, M. R. and Gaitonde, D. V. "High-Order Accurate Methods for Unsteady Vortical Flows on Curvilinear Meshes," AIAA Paper 98-0131, 1998.
25. Wasistho, B., Guerts, B. J. and Kuerten, J. G. M., "Simulation Techniques for Spatially evolving Instabilities in Compressible Flow over a Flat Plate," *Computers and Fluids*, Vol. 7, 1997, pp. 713-739.
26. Fung, K.-Y. and Ju, H. B., "Broadband Time-Domain Impedance Models," *AIAA Journal*, Vol. 39, No. 8, 2001, pp. 1449-1454.
27. Jenkins, L. N., Khorrami, M. R., and Choudhari, M., "Characterization of Unsteady Flow Structures Near Leading-Edge Slat: Part I. PIV Measurements," AIAA Paper 2004-2801, 2004.
28. Hammond, D. A. and Redekopp, L. G., "Global Dynamics of Symmetric and Asymmetric Wakes," *J. Fluid Mech.,* Vol. 331, 1997, pp. 231-260.
29. Woodley, B. M. and Peake, N., "Global Linear Stability Analysis of Thin Aerofoil Wakes," *J. Fluid Mech.*, Vol. 339, 1997, pp. 239-260.

30. Brentner, K. S., "Prediction of Helicopter Discrete Frequency Rotor Noise - A Computer Program Incorporation Realistic Blade Motions and Advanced Acoustic Formulation," NASA TM-87721, 1986.
31. Kurze, U. J. and Allen, C. H., "Influence of Flow and High Sound Level on the Attenuation in a Lined Duct," *J. Acoust. Soc. Amer*, Vol. 49, No. 5, 1971, pp. 1643-1654.